AGU PUBLICATIONS

JGR

Journal of Geophysical Research: Solid Earth

RESEARCH ARTICLE
10.1002/2013JB010765

Key Points:
- Invert for slip rate of San Andreas Fault using 3-D earthquake cycle model
- Viscoelasticity can explain discrepancy between geologic and geodetic slip rate
- Infer 60 km elastic plate over viscoelastic half-space (10^{19} Pa s)

Supporting Information:
- Readme
- Table S1

Correspondence to:
X. Tong,
xitong@ucsd.edu

Citation:
Tong, X., B. Smith-Konter, and D. T. Sandwell (2014), Is there a discrepancy between geological and geodetic slip rates along the San Andreas Fault System?, *J. Geophys. Res. Solid Earth*, *119*, doi:10.1002/2013JB010765.

Received 11 OCT 2013
Accepted 23 FEB 2014
Accepted article online 27 FEB 2014

Is there a discrepancy between geological and geodetic slip rates along the San Andreas Fault System?

Xiaopeng Tong[1], Bridget Smith-Konter[2], and David T. Sandwell[1]

[1]Scripps Institution of Oceanography, University of California, San Diego, La Jolla, California, USA, [2]Department of Geology and Geophysics, University of Hawai'i at Mānoa, Honolulu, Hawaii, USA

Abstract Previous inversions for slip rate along the San Andreas Fault System (SAFS), based on elastic half-space models, show a discrepancy between the geologic and geodetic slip rates along a few major fault segments. In this study, we use an earthquake cycle model representing an elastic plate over a viscoelastic half-space to demonstrate that there is no significant discrepancy between long-term geologic and geodetic slip rates. The California statewide model includes 41 major fault segments having steady slip from the base of the locked zone to the base of the elastic plate and episodic shallow slip based on known historical ruptures and geologic recurrence intervals. The slip rates are constrained by 1981 secular velocity measurements from GPS and L-band intereferometric synthetic aperture radar. A model with a thick elastic layer (60 km) and half-space viscosity of 10^{19}Pa s is preferred because it produces the smallest misfit to both the geologic and the geodetic data. We find that the geodetic slip rates from the thick plate model agrees to within the bounds of the geologic slip rates, while the rates from the elastic half-space model disagree on specific important fault segments such as the Mojave and the North Coast segment of the San Andreas Fault. The viscoelastic earthquake cycle models have generally higher slip rates than the half-space model because most of the faults along the SAFS are late in the earthquake cycle, so today they are moving slower than the long-term cycle-averaged velocity as governed by the viscoelastic relaxation process.

1. Introduction

Geodesy has become an increasingly important tool for recovering crustal strain rates in tectonically active regions. In California, the high-accuracy GPS velocity field from continuous and campaign networks, such as the Plate Boundary Observatory (PBO) and Southern California Integrated GPS Network (SCIGN), and field surveys have been used to estimate fault slip rates along the San Andreas Fault System (SAFS) [*McCaffrey*, 2005; *Meade and Hager*, 2005; *Bird*, 2009; *Zeng and Shen*, 2014], especially for those faults where geological estimation is lacking or inaccurate. The long-term fault slip rates on these major faults are an important component in earthquake hazard analysis because one can estimate moment accumulation rate when combined with estimates of the seismogenic depth.

The common approach for inverting for fault slip rates is through application of elastic half-space models [e.g., *McCaffrey*, 2005]. An important assumption in the half-space model is that the observed velocity field is steady over time, and the transient effects from past earthquakes can be neglected. This assumption is valid if the relaxation times of the lower lithosphere are much larger than half of the recurrence interval of a given fault [e.g., *Meade and Hager*, 2005]. When this model applies to three-dimensional problems, the interseismic velocity field can be explained by a combination of rigid block rotations with kinematically consistent fault slip rates and fault locking within the interseismic period.

Recent studies [e.g., *Bird*, 2009; *Zeng and Shen*, 2014] suggest an apparent discrepancy between the geologic and geodetic slip rates along the SAFS, although the uncertainties resulting from both of these estimates are quite large. The fault segments that are currently in debate include the following: the Imperial Fault [*Dawson and Weldon*, 2013] the southernmost San Andreas Fault and the San Jacinto Fault [*Van der Woerd et al*., 2006; *Lundgren et al*., 2009; *Lindsey and Fialko*, 2013], the San Bernardino segment [*Loveless and Meade*, 2011; *Spinler et al*., 2010; *McGill et al*., 2013], the Mojave segment [*Savage and Lisowski*, 1998; *Chuang and Johnson*, 2011], the Eastern California Shear Zone [*Oskin et al*., 2008], the creeping section [*Titus et al*., 2006; *Toké et al*., 2011], and the Peninsular segment of the San Andreas Fault [*Geist and Andrews*, 2000; *McCaffrey*, 2005].

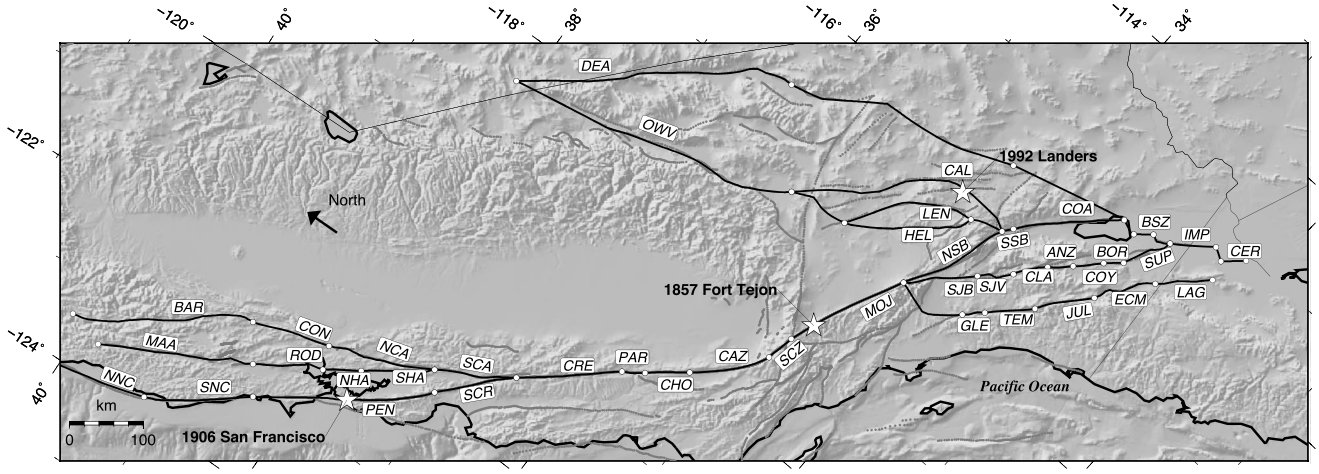

Figure 1. A regional topography map of the San Andreas Fault System in California shown in an Oblique Mercator projection. The projection pole (−74.4°W, 50.1°N) is from *Wdowinski et al.* [2007]. The black lines represent the fault segments studied in this paper. Each fault segment is labeled by a three-character name (Table 1). The white stars represent three major earthquakes that are believed to cause significant postseismic relaxation in the lower crust and upper mantle.

The discrepancy can be possibly resolved by introducing viscoelastic relaxation [*Nur and Mavko*, 1974; *Savage and Prescott*, 1978] to the interseismic velocity modeling. It has been observed that following large earthquakes, steady state crustal motion is perturbed by the viscoelastic response: the surface strain rate will increase immediately following an event and diffuse away slowly over years or decades. The 1906 San Francisco earthquake and the 1857 Fort Tejon earthquake may have had a long-lasting postseismic effect depending on the rheological properties of the lithosphere [*Savage and Lisowski*, 1998; *Pollitz et al.*, 2004]. A range of viscosity structures have been estimated from postseismic deformation following recent $M > 7$ earthquakes [*Pollitz et al.*, 2001; *Kenner and Segall*, 2003; *Freed and Bürgmann*, 2004; *Smith and Sandwell*, 2004]. Previous studies with similar objectives [*Dixon et al.*, 2002, 2003; *Johnson et al.*, 2007; *Lundgren et al.*, 2009; *Chuang and Johnson*, 2011] have been focused on either a few key fault segments or Southern California, and questions remain to be addressed in a California statewide three-dimensional model that integrates recently assembled GPS and intereferometric synthetic aperture radar (InSAR)-derived velocities and paleoseismology data.

The goal of this study is to estimate fault slip rates of the SAFS spanning the entire state of California using both a viscoelastic coupling model and an elastic half-space model to answer the following questions: How do the fault slip rates inferred using geodesy compare to the geological estimates? Along which fault segment of the SAFS are the geodetic and geologic slip rates incompatible? Can these discrepancies be reconciled by the viscoelastic earthquake cycle model? In order to answer these questions, we utilize a large data set including GPS velocity data, InSAR line-of-sight (LOS) velocity data, and geological data to construct a high-resolution deformation model of the SAFS, spanning the Cerro Prieto Fault to the south to the Maacama Fault to the north (Figure 1). We simultaneously solve for the long-term fault slip rates of 41 major faults using a three-dimensional earthquake cycle model. Then we focus on key faults where discrepancies between the geodetic and geologic slip rates are significant.

2. Data

2.1. GPS Velocities

The GPS data used in this study include 1981 horizontal velocity vectors covering major faults along the SAFS (Figure 2). There are 1863 velocity vectors used from the Uniform California Earthquake Rupture Forecast version 3 (UCERF3) GPS velocity solutions (T. Herring, personal communication, 2013). The velocity field is based on numerous GPS surveys and continuous GPS observations from the Plate Boundary Observatory (PBO) and Southern California Integrated GPS Network (SCIGN) projects used in the Southern California Earthquake Center (SCEC) Crustal Motion Model (CMM4) [*Shen et al.*, 2011], and the Making Earth System Data Records for Use in Research Environments (MEaSUREs) Solid Earth Science ESDR System [*Bock et al.*, 2011].

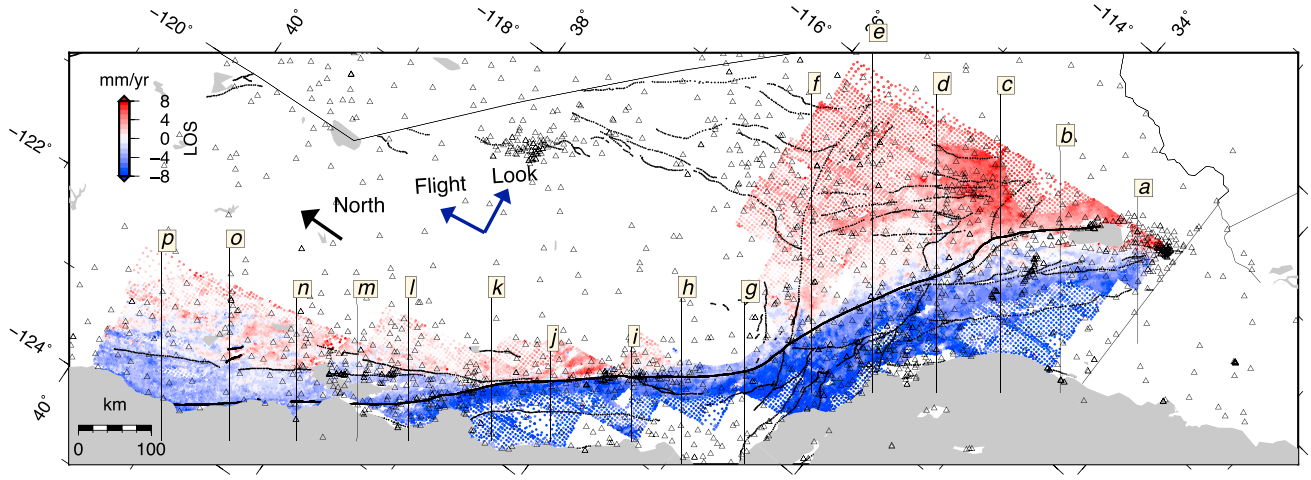

Figure 2. GPS stations (triangles) and InSAR LOS velocity data points (colored grid) along the SAFS in California, shown in Oblique Mercator projection. The InSAR data spans 4.5 years (2006.5–2011) and are derived from 1100 Advanced Land Observing Satellite (ALOS) radar interferograms. The radar flight direction (ascending) and look direction are provided. Positive velocities (red) represent ground motion away from the satellite. The geological fault traces are shown as black lines. The thin black lines with letter labels corresponds to the profiles shown in Figures 7a and 7b.

When modeling the interseismic velocity field, it is important to keep in mind how the GPS solutions are derived and what they represent. The GPS velocities used for this study span the years from 1996 to present. Secular velocity terms are estimated, along with any postseismic signals (logarithmic functions) for the events after 1996. The postseismic signals from earthquakes before 1996, such as the 1992 Landers earthquake, the 1906 San Francisco earthquake, and the 1857 Fort Tejon earthquake, were not accounted for in the GPS data analysis (T. Herring, personal communication, 2013). In this study, we correct the secular velocity field solution for postseismic relaxation following the 1992 Landers earthquake using a slip model from *Fialko* [2004]. Our model predicts that the postseismic velocity after approximately 20 years of the Landers earthquake is ~1.5 mm/yr at maximum for the sites surrounding the rupture. This corrected secular velocity field is used in the slip rate inversion. The postseismic relaxation from the 1906 and 1857 events and other past earthquakes are treated systematically in our earthquake cycle model (section 3).

In addition, we added velocities from eight campaign sites in Central California [*Rolandone et al*., 2008] that cover the central portion of the creeping section. A new velocity field from 110 campaign sites near Salton Trough in Southern California [*Crowell et al.*, 2013] was also included to provide a dense coverage of the near-fault deformation near the Imperial Fault. Both of the campaign GPS results were rotated into the reference frame of the continuous GPS sites to yield a consistent velocity field. Because these GPS solutions are different in terms of observation duration, uncertainties, and processing technique, we quantify their importance by assigning a weighting factor to the different data sets. The weight to the GPS data set from T. Herring is 1. We used a weight for the campaign data set from *Rolandone et al*. [2008] and *Crowell et al.* [2013] of 0.5 and 0.33, respectively, because of relatively short observation periods of each. We focus on the horizontal GPS velocity data only; no vertical velocities were used in this study.

2.2. InSAR LOS Velocities

The InSAR data used in this study were obtained through an L-band radar onboard Advanced Land Observing Satellite (ALOS) launched by Japanese Space and Exploration Agency (JAXA), which can maintain good temporal coherence in vegetated areas compared to C-band radar. The InSAR data (spanning 4.5 years from 2006.5 to 2011) were acquired along the ascending orbits 34° look angle). The InSAR LOS velocities (Figure 2) were derived from integration of the radar interferogram stacking and GPS velocities [*Tong et al*., 2013]. In this previous study, the long wavelength of the velocity field (>40 km) was constrained by GPS, and InSAR was used to retrieve the short wavelength (<40 km) features of the deformation spectrum. The crossover wavelength is determined by a coherence spectrum analysis. A detailed description of the integration method can be found in *Tong et al*. [2013]. The main contribution of the InSAR data is to recover details of the aseismic fault creep on the creeping section and other faults along the SAFS.

Journal of Geophysical Research: Solid Earth

10.1002/2013JB010765

Table 1. Summary of the Fault Segments, Locking Depths, Past Earthquakes, Geologic, and Geodetic Fault Slip Rates of the SAFS[a]

Fault Label	Fault Name	Recurrence Interval (years)	Date of the Historical Earthquakes	Locking Depth (km)	Preferred Geologic Slip Rate (mm/yr)
CER	Cerro_Prieto	200	1825 1915 1927 1934 1966	10.0	35
IMP	Imperial	200	1525 1575 1650 1700 18 5 1915 1940 1979	5.9	35
BSZ	Brawley	200	1700 1875 1906 1979	12.0	25
COA	Coachella	200	774 824 982 1020 1107 1230 1300 1347 1475 1503 1683	11.5	20
SSB	South_San_Bernardino	200	77 824 982 1020 1107 1230 1300 1347 1475 1503 1683 1987	16.4	13
NSB	North_San_Bernardino	200	774 931 1173 1107 1313 1347 1450 1475 1500 1619 1684 1704	17.8	19
SUP	Superstition_Hills and Superstition Mount combined	600	1050 1460 1540 1987	10.8	11
BOR	Borrego_Mountain	550	1050 1460 1540 1987	10.0	5
COY	Coyote_Creek	500	1892 1968	10.0	5
ANZ	Anza	300	1892 1942 1954 1968 1969 1987	10.0	14
CLA	Clark	300	1020 1230 1290 1360 1630 1760	12.0	8
SJV	SJ_Valley	450	1770 1899 1918	15.0	16
SJB	SJ_San Bernadino Valley	500	1770 1923	15.0	6
MOJ	Mojave	220	533 634 697 722 781 850 1016 1116 1264 1360 1487 1536 1685 1812 1857	15.0	34
SCZ	S_Carrizo (Big Bend)	250	599 1078 1247 1277 1310 1384 1393 1417 1457 1462 1565 1571 1614 1713 1749 1857	15.0	34
CAZ	Carrizo	200	599 1078 1247 1277 1310 1384 1393 1417 1457 1462 1565 1571 1614 1713 1749 1857	15.0	34
CHO	Cholame	200	1857	12.0	34
PAR	Parkfield	20	1857 1881 1901 1922 1934 1966	12.0	34
CRE	Creeping	250	NA	12.0	34
SCR	Santa_Cruz_Mt	150	1300 1600 1838 1890 1906 1989	12.0	17
PEN	SA_Peninsula	230	1300 1600 1838 1906	16.2	17
SNC	S_SA_N_Coast	230	1300 1600 1906	15.5	24
NNC	N_SA_N_Coast	270	1300 1600 1899 1906	13.2	24
SCA	S._Calaveras	300	1864 1897 1911 1984	12.0	15
NCA	N._Calaveras	550	1864	12.0	6
CON	Concord	3000	510	12.0	4.3
BAR	Hunting Creek/Bartlett Spring	500	1760	12.0	4
SHA	S._Hayward	200	1470 1630 1730 1868	12.0	9
NHA	N._Hayward	300	1708	12.0	9
ROD	Rodgers_Creek	400	1898	12.0	9
MAA	Maacama	250	NA	12.0	9
LAG	Laguna_Salada	1000	1892	9.0	3
GLE	Elsinore_GlenIvy	1000	963 1230 1283 1440 1627 1850 1910	10.0	5
TEM	Elsinore_Temecula	1000	1655 1810	10.0	5
JUL	Elsinore_Julian	1500	1655 1680 1753 1804	10.0	3
ECM	Elsinore_Coyote_Mt	1500	1650 1892	10.0	3
LEN	Lenwood-Lockhart-Old Woman Springs	3000	1100	12.0	1
HEL	Helendale	3000	1100	12.0	0.6
CAL	Calico-Hidalgo	3000	510	10.0	1.6
OWV	Owens_Valley	3000	1100 1872	11.5	3.5
DEA	Death_Valley	1000	1100	12.0	3

Journal of Geophysical Research: Solid Earth

10.1002/2013JB010765

Table 1. (continued)

Fault Label	Bounds on the Geological Slip Rates (mm/yr)	Geodetic Slip Rate From HS Model (mm/yr)	Uncertainties of the Geodetic Slip Rate From HS Model (mm/yr)	Geodetic Slip Rate From PL6019 Model (mm/yr)	Uncertainties of the Geodetic Slip Rate From PL6019 Model (mm/yr)	Geodetic Slip Rate From PL3019 Model (mm/yr)	Uncertainties of the Geodetic Slip Rate From PL3019 Model (mm/yr)	Geodetic Slip Rates From PL3020 Model (mm/yr)	Uncertainties of the Geodetic Slip Rates From PL3020 Model (mm/yr)
CER	30–40	42.1	0.8	41.7	0.8	37.1	0.7	39.5	0.8
IMP	15–40	44.1	1.0	44.0	1.0	43.0	1.0	43.9	1.0
BSZ	15–30	23.5	0.5	24.6	0.5	32.7	0.5	30.7	0.5
COA	15–30	19.7	0.5	19.5	0.5	19.6	0.6	22.8	0.5
SSB	5–20	17.4	0.2	21.1	0.5	25.5	0.7	19.2	0.4
NSB	13–28	16.0	0.4	15.2	0.4	13.5	0.5	14.1	0.5
SUP	4–15	11.4	0.5	16.7	0.6	13.2	0.6	13.9	0.6
BOR	1–10	7.1	0.3	10.8	0.3	14.3	0.3	9.1	0.3
COY	1–10	8.9	0.4	10.6	0.4	11.9	0.4	8.8	0.4
ANZ	11–18	15.1	0.3	16.4	0.3	16.9	0.4	14.7	0.3
CLA	6–11	10.1	0.4	9.7	0.4	8.7	0.4	8.9	0.5
SJV	12–24	15.1	0.5	15.9	0.5	17.8	0.4	16.4	0.4
SJB	2–8	4.6	0.5	5.9	0.5	12.4	0.6	7.8	0.6
MOJ	25–40	25.5	0.3	27.8	0.3	33.1	0.4	22.9	0.3
SCZ	31–37	36.2	0.3	36.3	0.3	36.9	0.3	31.7	0.3
CAZ	31–37	36.2	0.3	36.3	0.3	37.2	0.3	33.1	0.3
CHO	29–39	32.2	0.2	33.0	0.2	34.5	0.2	32.4	0.2
PAR	26–39	34.0	0.5	34.9	0.5	37.7	0.5	35.0	0.5
CRE	29–39	34.5	0.3	38.7	0.4	43.8	0.4	36.3	0.4
SCR	13–21	15.7	0.5	17.1	0.5	19.7	0.5	17.2	0.5
PEN	13–21	18.1	0.4	20.5	0.4	25.4	0.4	17.6	0.4
SNC	16–27	14.0	0.4	23.0	0.5	36.5	0.7	33.2	0.6
NNC	16–27	19.0	0.7	22.2	0.9	21.3	1.0	20.0	0.9
SCA	10–20	16.1	0.3	19.5	0.3	21.0	0.4	19.0	0.3
NCA	3–8	9.0	0.3	10.4	0.4	10.0	0.5	9.0	0.4
CON	3–9	7.7	0.5	9.0	0.5	10.7	0.5	9.1	0.5
BAR	2–9	7.3	0.4	8.5	0.4	8.5	0.5	10.1	0.4
SHA	7–11	9.2	0.1	9.5	0.1	11.2	0.1	9.7	0.1
NHA	7–11	9.8	0.1	9.8	0.1	10.4	0.1	9.7	0.1
ROD	6–11	12.0	0.2	12.0	0.3	12.6	0.3	10.2	0.3
MAA	6–12	9.8	0.3	10.8	0.3	15.1	0.3	12.7	0.3
LAG	1–5	2.9	0.2	5.4	0.2	7.2	0.3	5.4	0.2
GLE	3–7	4.7	0.1	4.7	0.1	4.6	0.1	4.6	0.1
TEM	3–7	4.0	0.2	4.0	0.2	3.2	0.2	3.6	0.1
JUL	1–5	0.0	0.0	0.0	0.0	0.0	0.0	0.0	0.0
ECM	1–5	2.1	0.3	1.2	0.3	0.4	0.3	5.5	0.4
LEN	0.6–1.4	3.9	0.6	4.2	0.7	2.9	0.8	6.0	0.6
HEL	0.2–1.0	0.4	0.4	0.8	0.5	1.1	0.6	0.0	0.0
CAL	1.0–2.8	6.9	0.3	7.3	0.3	7.7	0.3	6.6	0.4
OWV	2–5	7.1	0.1	6.2	0.1	4.0	0.1	4.6	0.1
DEA	2–4	5.0	0.3	5.0	0.3	6.5	0.3	5.7	0.3

[a]See text for details [*Dawson and Weldon*, 2013].

For aspects of this study, we first made a mask for the InSAR LOS velocity data to isolate nontectonic effects. We identified 47 anomalous areas that exhibit anthropogenic-related ground motion, most likely caused by groundwater extraction, along the major faults in California. These anomalous areas are evident because they produce large-vertical motion either confined by known aquifers or bounded by fault stepovers. The data within these anomalous areas were not used. The remaining LOS velocity data were downsampled to 53,792 points based on the second invariant of the strain rates. This subsampled data set provides full resolution in high-velocity gradient area near the faults and lower resolution in areas of low strain rate far away from the faults. The three-component look vectors and the standard deviations for each LOS velocity data point were subsampled in the same manner. These InSAR data are available in the supporting information of this paper.

The uncertainties of the LOS velocities are larger than GPS measurements, typically 3–4 mm/yr. Data accuracy would be greatly improved if the ALOS mission had a longer duration and if a second LOS direction along descending orbits were available. The ALOS-2 mission, scheduled for launch on May 24th, 2014, will provide more frequent data collection along two look directions, so future data will likely resolve these issues.

2.3. Geological Data

The fault slip rates of closely spaced parallel faults such as the Elsinore, San Jacinto, and San Andreas in Southern California and the San Andreas, Maacama, and Green Valley faults in Northern California are difficult to resolve using geodesy alone. To make a kinematically consistent model, we introduced three types of geological conditions to loosely constrain the fault slip rates. First, we attempted to constrain the recovered slip rate to be within the upper and lower bounds of the quaternary fault slip rates. The quaternary fault slip rates used in this study are from the Working Group on California Earthquake Probabilities (WGCEP) [*Dawson and Weldon*, 2013]. We assigned each estimate an uncertainty to account for the variability in quaternary fault slip rate derived by different investigators compiled in Appendix B in UCERF3 (Table 1). Second, we introduced a closure criterion at fault branching points such that where two fault strands join into a single strand, the sum of the two strand rates should match the single strand rate. This condition has an analog to the classic triple junction closure criteria at plate intersections. Third, we required that the sum of slip rates on parallel strands should approximately match the overall relative slip rate along the plate boundary (e.g., ~ 45 mm/yr).

In order to make a fair comparison between the recovered geodetic slip rates and the geological estimates, we treated the geological constraint with caution. The best approach we found was to apply a weighting parameter in the inversion to quantify the significance of the geological constraints. The best fit weight for the geological constraints was found through a grid search (see section 4 for details). In fact, this approach can be deemed as conservative because the recovered geodetic slip rates are required to match the geologic slip rates in the inversion. Thus, the difference between the geologic and geodetic slip rate results is more likely to be caused by real discrepancy instead of nonuniqueness inherent in the inversion.

3. Earthquake Cycle Model

To calculate surface velocities from locked faults, we used a fully three-dimensional, time-dependent earthquake cycle model [*Savage and Prescott*, 1978; *Smith and Sandwell*, 2004, 2006]. The model comprises an elastic (plate) layer overlying a viscoelastic half-space (here we refer to it as the "plate model" in contrast to the "half-space model"). The earthquake cycle effect produces time-dependent deformation by viscoelastic relaxation of the asthenosphere. This model assumes a linear rheology of the viscous layer corresponding to diffusion creep in the laboratory-derived flow law.

Figure 3a shows an example of the surface interseismic velocity predicted by our earthquake cycle model [*Smith and Sandwell*, 2006]. Figure 3b is a schematic diagram depicting key features in this model. The difference between this model and the elastic model are temporal variations of the present-day surface velocity. When the observation time is earlier than the relaxation (or Maxwell) time, which is defined as twice the effective viscosity divided by the shear modulus (assumed to be 30 GPa throughout the study), the velocity is generally higher than the cycle average (gray line), while for later times (when the observation time is significantly later than the Maxwell time), the velocity is generally lower than the cycle average. This comparison serves as a validation of our three-dimensional forward model against the two-dimensional (2-D) analytic solutions from *Savage and Prescott* [1978]. What derivates from the original 2-D model is that we incorporated realistic curved faults in our three-dimensional (3-D) model and we used appropriate earthquake sequences based on geologic records.

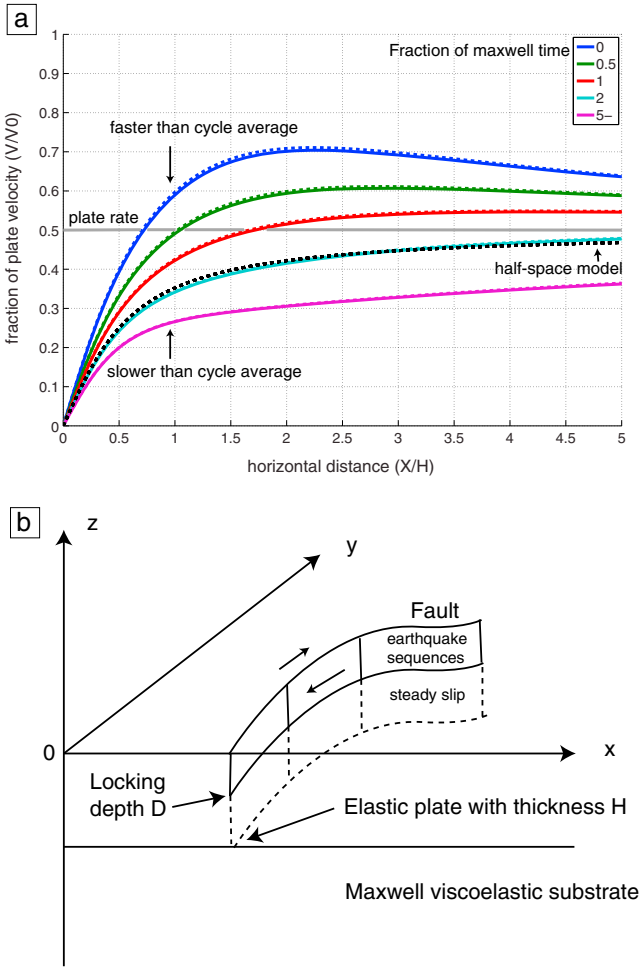

Figure 3. (a) Comparison between our numerical earthquake cycle model (solid lines) and 2-D analytic models (dashed lines) [*Savage and Prescott*, 1978]. The cross sections of the fault-parallel velocity at the surface are shown. We considered a 60 km thick plate with an effective viscosity of approximately 10^{19} Pa s in this comparison. The fault slips at plate rate from the locking depth (15 km) to the bottom of the elastic plate. We prescribed 20 earthquakes with a recurrence interval of 100 years. The time is normalized by the Maxwell time (20 years). The colored lines represent different time periods during the earthquake cycle. It is clear that the numerical model accurately reproduces the analytical solution at different times within an earthquake cycle. (b) Schematic figure showing that our model simulates viscoelastic effects using realistic earthquake sequences and arbitrary fault geometry in three dimensions.

Compared to the 2-D model, the 3-D model predicts a reduced viscoelastic effect. Viscoelastic relaxation is proportional to the length of the fault segment; thus, only significant earthquakes produce long-lasting transient deformation. This model is different from the traditional block models that use the "back slip" approach [*McCaffrey*, 2005; *Meade and Hager*, 2005; *Chuang and Johnson*, 2011] in that this model characterizes earthquake cycle deformation on faults as buried dislocations along block boundaries (i.e., "forward slip") to account for the interseismic locking effect. The time-dependent strain concentration near the fault is produced by transient effect in the viscoelastic mantle [*Smith and Sandwell*, 2006].

In this model, the right-lateral shear between the North American and Pacific plates is taken up by several major strike-slip faults (Figure 1). In the long term, the crust is displaced at the fault boundaries, behaving like rigid blocks. We restricted our analysis to the fault geometry adopted from *Smith-Konter and Sandwell* [2009]. The modeled faults include the entire trace of the San Andreas faults from Point Arena to Bombay Beach: the San Jacinto fault, Elsinore fault, Imperical fault, and Cerro Prieto Fault in Southern California; the Hayward fault, Calaveras Fault, Rodgers Creek fault, Maacama Fault, Hunting Creek-Bartlett Springs fault, and Concord Fault in Central and Northern California. In East California Shear Zone, we consider the Lenwood-Lockhart-Old

Table 2. Fit to GPS, InSAR, and Geologic Data for Four Different Rheological Models

Model	HS	PL6019	PL3019	PL3020
GPS χ^2 misfit	2.67	2.56	2.74	2.68
GPS WRMS (mm/yr)	1.71	1.68	1.73	1.72
InSAR χ^2 misfit	0.28	0.27	0.27	0.28
InSAR WRMS (mm/yr)	1.34	1.30	1.31	1.34
RMS to the preferred geologic slip rate (mm/yr)	3	3	5	4

Woman Springs fault, Helendale fault, and Calico-Hidalgo fault. We also include the Owens Valley fault and Death Valley fault with an aim to balance the slip budget across the plate boundary.

In summary, the fault model consists of 41 fault segments, each having uniform slip rate, locking depth, and earthquake history. Each segment is further subdivided into smaller patches (~ 5 km length) following the curvature of the fault trace at surface. Each fault segment slips at a steady velocity from its locking depth to the base of the elastic plate. Coseismic ruptures are assumed to extend from the surface to the locking depth prescribed for each fault segment. The locking depth of each fault is estimated by the seismogenic depth and GPS observations [*Smith-Konter et al*., 2011].

Our experiment explores four different rheological models: an elastic half-space model and three elastic plate models (Table 2). We experimented two possible thicknesses (thick versus thin) for the elastic layer in an attempt to understand the behavior of viscoelastic relaxation in relation to the lithosphere's rheology. The half-space model has localized steady slip from the locking depth to infinite depth. In contrast, the plate models have localized slip from the locking depth extending to the base of the elastic layer. This localized steady slip surface in the crust and upper mantle is a kinematic description, and we did not attempt to simulate the stress-driven creep within the fault zone [e.g., *Hetland et al*., 2010]. It is noticeable that the elastic strain in the interior of the block from the plate model is significantly greater than that from the half-space model.

We note that the earthquake reoccurrence along many fault segments of the SAFS is irregular, based on the paleoseismological record. Oversimplification of the earthquake sequence using a characteristic earthquake model may not be appropriate. We used realistic earthquake sequences based on a recent compilation of all the historical and prehistorical earthquakes dated from the year 1000 to present [*Smith and Sandwell*, 2006, and references therein; *Solis*, 2013] to "spin up" the earthquake cycle. When the information on the past earthquake sequences are lacking, we prescribed periodic earthquake cycles according to the estimated recurrence interval [*Dawson and Weldon*, 2013]. Because the magnitude of the slip along each segment for each event is usually not known, we assume that the shallow slip events "catch up" with the deep slip over an earthquake cycle to satisfy block motion on the fault. This earthquake recurrence concept is directly derived from the slip-predictable model. In section 6.1, we investigate the effect of this slip-predictable assumption in detail.

The dislocation based earthquake cycle model does not include aseismic creep in the upper crust. It is generally thought that the fault creep is confined within the shallowest sedimentary layer of the crust (1 or 2 km depth). However, it has been found that fault creep can occur within the brittle upper crust along several major faults in Central and Northern California [*Rolandone et al*., 2008]. We augmented this model using shallow dislocations in an elastic half-space [*Wang et al*., 2003]. The creeping faults modeled in this study include the Hayward, Calaveras, Maacama, Concord, Bartlett Springs, Rodgers Creek fault, Parkfield, the creeping segment, and Santa Cruz Mountain segment of the San Andreas Fault of the Northern SAFS and the Imperial, Superstition Hills, and the Brawley Seismic Zone of the Southern SAFS [*Tong et al*., 2012]. These fault segments are discretized into small rectangular dislocation patches extending from the surface to 12 km deep in the upper crust. We jointly solved for the aseismic creep rates of these fault segments along with 41 long-term fault slip rates in the inversion as described in the next section. The details of the aseismic creeping faults deserve further study but this work is out of the scope of this paper.

4. Inversion Method

In this section, we describe the system of linear equations used to estimate slip rates on 41 fault segments $\overline{s}$ and 66 creep rates $\overline{p}$ from a combination of 1981 GPS vector velocity measurements $\overline{v_g}$, 53,792 line-of-sight

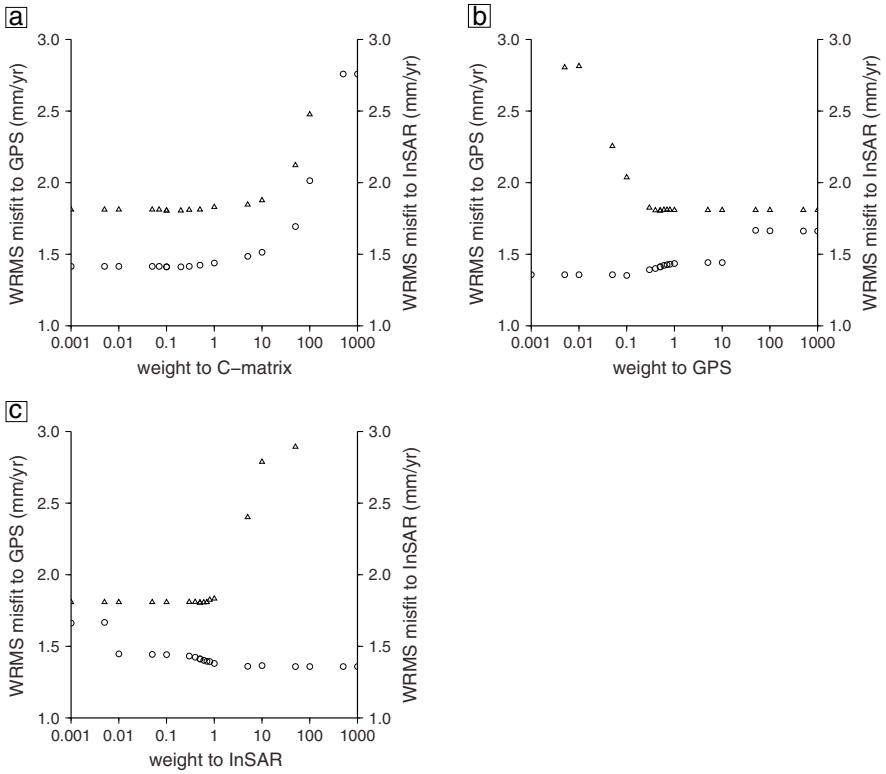

Figure 4. Grid search to determine the relative weighting factors used in the inversion. (a) Weight to the C-matrix, (b) weight to GPS, and (c) weight to InSAR. The triangles are the weighted RMS misfit to the GPS data and the circles are the weighted RMS misfit to the InSAR data. The actual weights used in the slip rate inversion are 0.3 for GPS, 0.2 for InSAR, and 0.1 for the geological constraint.

(LOS) InSAR measurements $\bar{l}$, and geologic constraints. This linear system consists of four subsystems of equations representing the GPS data, InSAR data, geological constraints, and smoothing constraints, respectively:

$$\begin{bmatrix} \overline{\overline{G_g}} & \overline{\overline{E_g}} & \bar{\bar{I}} & \bar{\bar{r}} \\ \overline{\overline{G_i}} & \overline{\overline{E_i}} & \bar{\bar{I}} & \bar{\bar{r}} \\ \overline{\overline{C}} & 0 & 0 & 0 \\ 0 & \overline{\overline{S}} & 0 & 0 \end{bmatrix} \begin{bmatrix} \bar{s} \\ \bar{p} \\ \overline{v_0} \\ \overline{w} \end{bmatrix} = \begin{bmatrix} \overline{v_g} \\ \bar{l} \\ \overline{s_c} \\ 0 \end{bmatrix}, \tag{1}$$

where $\overline{\overline{G}}$ and $\overline{\overline{E}}$ are the Green's function for modeled surface velocity. The subscripts *g* and *i* refer to GPS and InSAR data, respectively. $\overline{\overline{G}}$ is derived from the earthquake cycle model and depends on the elastic plate thickness, effective viscosity, locking depth of the fault, and the earthquake sequence of the segment [*Smith and Sandwell*, 2004]. $\overline{\overline{E}}$ is derived from the dislocation model depending on the elastic property of the material. $\overline{\overline{C}}$ is the constraint matrix, which includes the geologic slip rate estimates, the triple junction closure constraint, and the far-field velocity constraint. $\overline{\overline{S}}$ is the smoothing matrix applied only to the shallow dislocations representing the aseismic creep. In order to separate the effect of the plate rotation from the interseismic signal, we introduce $\overline{v_0}$ and $\overline{w}$, representing the translation term and the rotation term of the velocity field in a Cartesian coordinate. $\overline{v_0}$ has two unknowns denoting two translation terms in the east and north velocities. $\overline{w}$ describes the rotation rate (one unknown) around a prescribed rotation axis that is orthogonal to the east and north velocity direction. $\bar{\bar{r}}$ represents the location of the velocity measurements with respect to the rotation axis. We do not intend to solve for the location of the rotation axis and the rotation rate simultaneously because of the strong trade-offs between these two quantities. $\bar{\bar{I}}$ is the identify matrix. After running the inversion, we found that the rotation term $\overline{w}$ can absorb the residuals of the observed velocity field although it is relatively small in this particular tectonic setting.

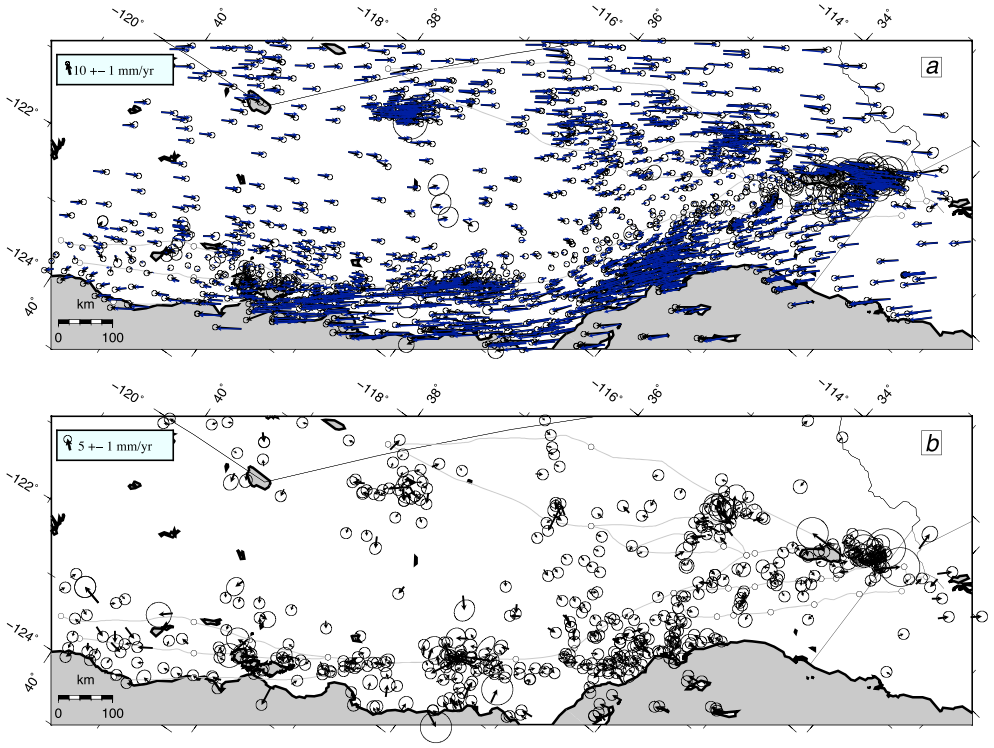

Figure 5. Results of model fit to the GPS data. (a) Model and data horizontal velocities. The black arrows show the observed GPS horizontal velocity vectors with 95% confidence interval. The blue arrows show the predicted horizontal velocity vectors from the preferred plate model PL6019. (b) GPS residual (observation-model) velocity vectors. Note the different scales used in the two figures. The thin gray curves denote the fault segments.

In the second subsystem that incorporates InSAR data, variable look vectors in the east and north component are used to project the horizontal velocity into radar line-of-sight direction even though they are not shown explicitly in equation (1). The third subsystem $\overline{\overline{C}}\,\bar{s} = \overline{s_c}$ represents three types of geological constraints represented by the following three matrix: $\bar{\bar{I}}$, $\overline{\overline{C_{\text{tot}}}}$, and $\overline{\overline{C_{\text{tri}}}}$, respectively. (1) Matrix $\bar{\bar{I}}$ denotes the estimates of slip rate from the geologic data $\overline{s_{\text{geol}}}$ on 41 segments; (2) matrix $\overline{\overline{C_{\text{tot}}}}$ represents the constraint that the sum of slip rate on subparallel fault strands must equal the total slip rate across the plate boundary ($\overline{s_{\text{tot}}} = 45$ mm/yr); (3) matrix $\overline{\overline{C_{\text{tri}}}}$ represents the constraint that at the fault junctions where two or more subparallel faults connect and converge into one main fault, the slip rate on the main fault must equal the sum of the subparallel faults ($\overline{s_{\text{tri}}} = 0$). We can represent this as follows:

$$\begin{bmatrix} \bar{\bar{I}} \\ \overline{\overline{C_{\text{tot}}}} \\ \overline{\overline{C_{\text{tri}}}} \end{bmatrix} \bar{s} = \begin{bmatrix} \overline{s_{\text{geol}}} \\ \overline{s_{\text{tot}}} \\ \overline{s_{\text{tri}}} \end{bmatrix}. \tag{2}$$

Equation (1) was normalized by the uncertainty in each component of the geodetic measurement. In addition, we introduced three weighting constants to the four subsystems of equations to have a sense of control on the slip rates solutions. The relative weights were determined by a grid search method to minimize the RMS misfit of the GPS and InSAR data (Figure 4).

We added Gaussian random noise to the input data and repeated the inversions 10 times. Then we computed the mean and the standard deviations as the final fault slip rate results. The amplitude of the random noise was chosen according to the uncertainties of the geodetic measurements. Like other studies [e.g., *McCaffrey*, 2005], we modified the formal uncertainties of the GPS data to have more realistic slip rate uncertainty estimates from the inversion. The minimum uncertainties of the GPS velocity measurements are set to be 1 mm/yr.

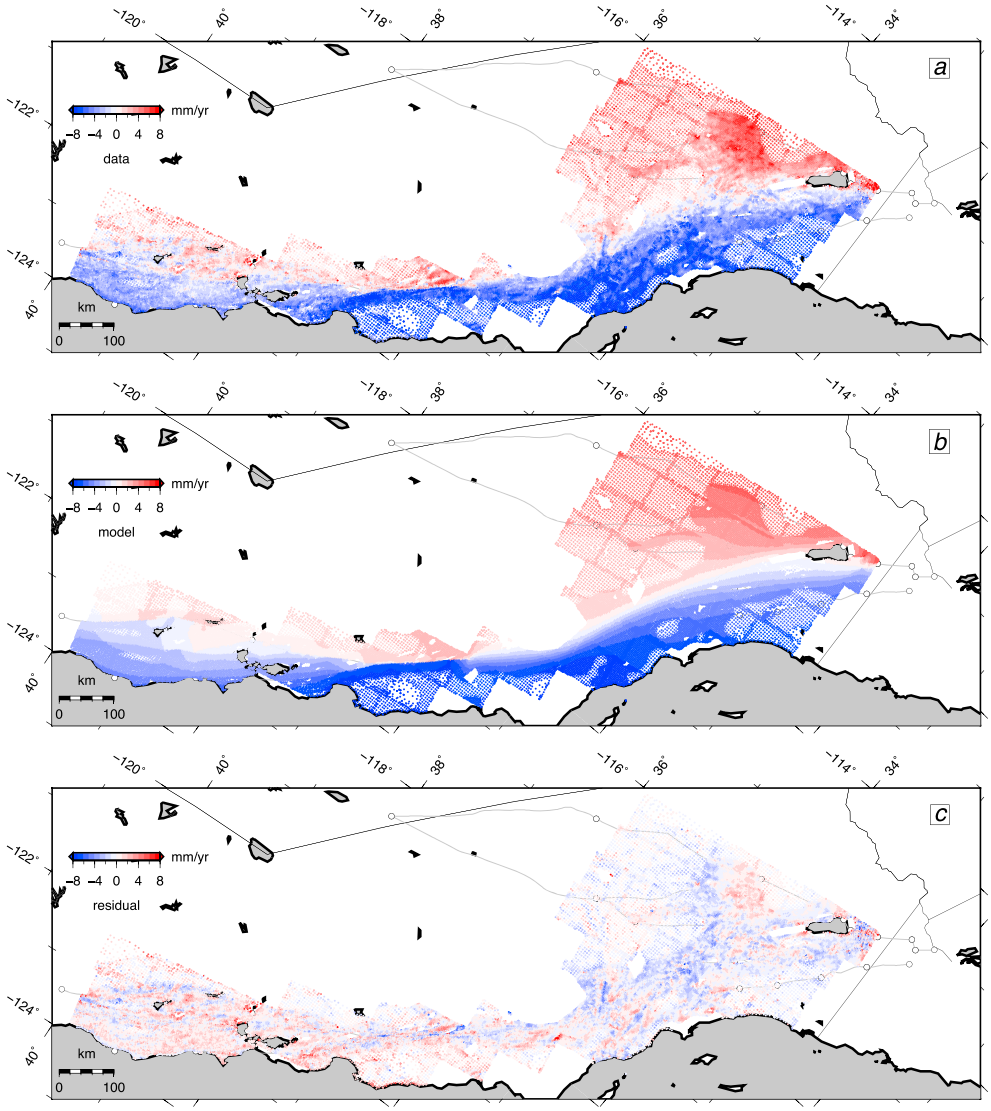

Figure 6. The fit to the InSAR LOS velocity data. Positive velocities (red) represent ground motion away from the satellite. The radar look direction and flight direction are marked in Figure 2. (a) Observed InSAR LOS velocity. (b) Predicted InSAR LOS velocity from the preferred plate model PL6019. (c) Residuals (observation-model) of the InSAR LOS velocity. The thin black curves denote the fault segments.

5. Results

5.1. The Quality of Fit

Table 2 shows the statistics of the misfits for four different rheological models: an elastic half-space (HS) model, a viscoelastic model with a relatively thick elastic plate (60 km) and moderate viscosity of 10^{19} Pa s (PL6019), a viscoelastic model with a thin elastic plate (30 km) and moderate viscosity of 10^{19} Pa s (PL3019), and a viscoelastic model with thin elastic plate (30 km) and relatively high viscosity 10^{20} Pa s (PL3020). The χ^2 misfit is defined as the squared sum of the residuals normalized by the standard deviation for each velocity measurement $\chi^2 = \frac{1}{N}\sum_{i=1}^{N}\left(\frac{o_i m_i}{\sigma_i}\right)^2$, where o_i is the data, m_i is the model, and σ_i is the uncertainties for N measurements. The χ^2 misfit to the entire GPS data set is 2.67 for HS, 2.56 for PL6019, 2.74 for PL3019, and 2.68 for PL3020 model assuming the formal uncertainties to be 1 mm/yr. The formal uncertainties of the InSAR data are probably overestimated; thus, the χ^2 misfit to InSAR are approximately 0.27.

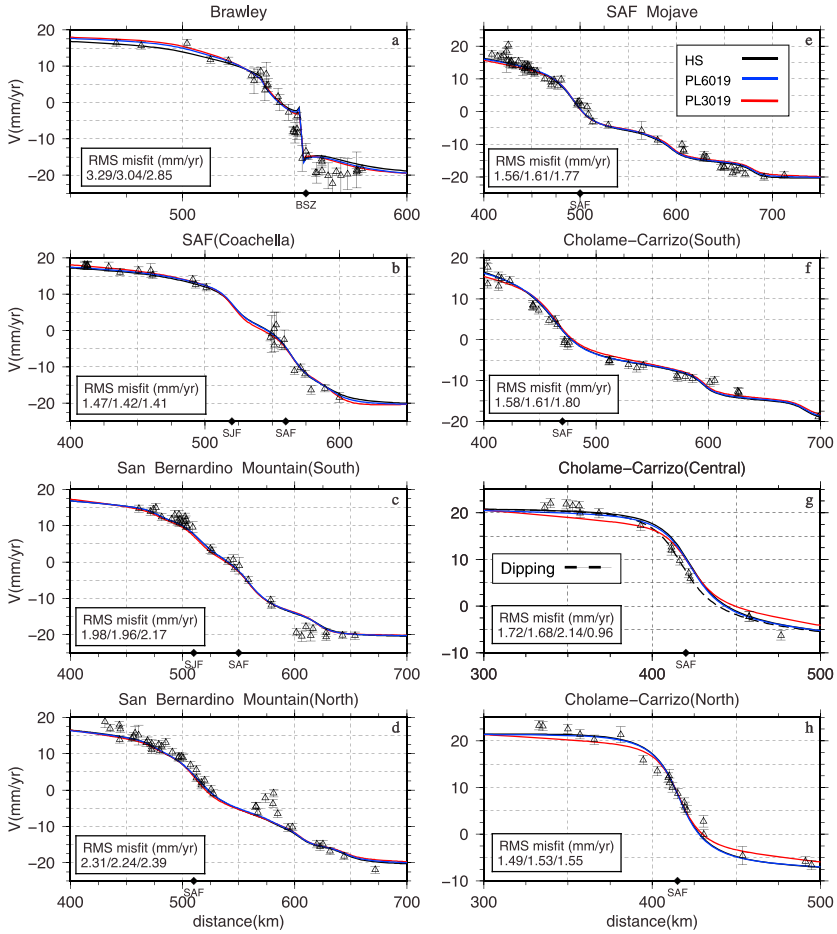

Figure 7. (a–h) Cross sections showing the GPS velocity data and its fit to the deformation models. The GPS velocity vectors are decomposed into two components (parallel and perpendicular to the plate motion) using an Euler pole (−74.4°W, 50.1°N). The parallel components are shown as triangles (with associated uncertainties) compared to the modeled velocity (solid lines). The profiles all run in N45°E direction (see Figure 2) and are labeled in the upper right corner of each subfigure. Three models are considered here: HS model (black line), PL6019 model (blue line), and PL3019 model (red line). The RMS misfit of each profile to the models is shown in the following order: HS/PL6019/PL3019. The locations of the major faults are labeled and marked by black diamonds at the bottom of each subfigure: BSZ: Brawley Seismic Zone, SAF: San Andreas Fault, SJF: San Jacinto Fault, HAY: Hayward fault, MAA: Maacama Fault, ROD: Rodgers Creek fault. The left side of each subfigure is the westside of the profiles. The error bars of the GPS data show one standard deviation. Inside profile g, we also tested a dipping fault model, shown as a dashed black line. See text for details. (i–p) Continuation of Figures 7a–7h.

In addition, we calculated the weighted RMS defined as $\mathrm{WRMS} = \sqrt{\frac{\sum_{i=1}^{N}\left(\frac{o_i - m_i}{\sigma_i}\right)^2}{\sum_{i=1}^{N}\frac{1}{\sigma_i^2}}}$. The weighted RMS residual to the entire GPS data set are found to be 1.71 mm/yr for the HS model, 1.68 mm/yr for the PL6019 model, 1.73 mm/yr for the PL3019 model, and 1.72 mm/yr for PL3020 model. The weighted RMS residuals to the InSAR data are less sensitive to different models: 1.34 mm/yr for the HS model, 1.30 mm/yr for the PL6019 model, 1.31 mm/yr for the PL3019 model, and 1.34 mm/yr for the PL3020 model. We found that the PL6019 model produced the smallest misfit to both of the GPS and InSAR data. The PL6019 model is marginally superior in matching observations to the PL3019 and PL3020 models, which indicates that the elastic thickness of the lithosphere underneath most of the SAFS is relatively thick. Different viscosities have minor influence on the model residuals.

Figure 5a shows the 1981 GPS velocity vectors and the predicted velocity from model PL6019. Our model is able to reproduce the right-lateral shear motion across the Pacific-North American plate boundary from the Cerro Prieto Fault to the south to the Maacama Fault to the north. The model captures the pronounced westward

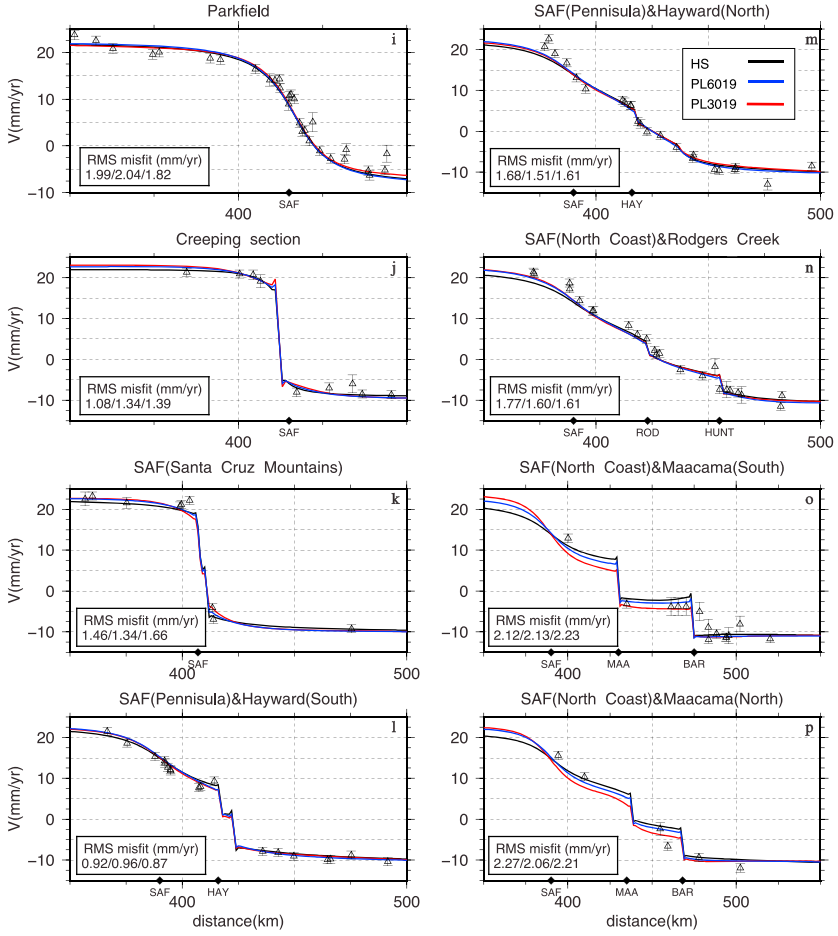

Figure 7. (continued)

rotation of the velocity field along the Big Bend and Mojave segment of the SAFS in large scale. Figure 5b shows the residual GPS velocity field for the same model PL6019. For illustrative purposes, only significant residuals that are greater than 2 times the standard deviations are shown. There are residuals along the southern tip of the creeping section and the Mojave Desert, which could be due to complicated postseismic signals from recent earthquakes. The residuals near the Channel Islands to the west of the California coast are probably caused by offshore faults not included in our model. In general, we found that the secular velocity field observed by GPS is explained well by this three-dimensional earthquake cycle model.

Figure 6 shows 53,792 InSAR LOS velocity point measurements, the prediction, and its residuals from model PL6019 (Table 2). The InSAR observations added in the inversion provides improved resolution of the near-fault ($<$10 km from the fault trace) deformation. Our model can reproduce both the broadscale deformation and the sharp velocity gradients at the creeping faults in California (See Figures 7a–7p).

In summary, the four models that we tested all yield satisfactory fit to the geodetic observations. From the resulting statistics, we determine that the quality of fit is not adequate to differentiate the plate models from the half-space model. In section 5.2, we investigate the half-space and plate models using profiles of the GPS velocity measurements. In section 5.3, we compare the geodetic slip rates from the four models to the geologic slip rates to identify statistically significant mismatches.

5.2. GPS Velocity Profiles

Figures 7a–7p show 16 fault-perpendicular velocity profiles at different locations along the SAFS (see Figure 2). These velocity profiles are plotted against the velocities predicted by the half-space (HS) model, a thick plate model (PL6019), and a thin plate model (PL3019). We decomposed GPS velocities into two

components, parallel and perpendicular to the plate motion, using an Euler pole (−74.4°W, 50.1°N). This pole is determined based on the pole of rotation analysis from *Wdowinski et al.* [2007]. The GPS fault-parallel velocity components (shown as triangles) are compared to the modeled fault-parallel velocity components (colored solid lines). We selected those GPS data that lie within 10 km of the northern and southern sides of each profile. Then we scrutinized the model misfits using the GPS data within the bounds of each profile. We have also tried to include more GPS data by enlarging the width of the profiles, but this increases the scatterness of the GPS velocities. Since the 3-D model has significant along-strike variations and the differences among the three models are subtle, we decided to limit the total geographical width reflected in our profiles to be 20 km. We computed a weighted RMS misfit for each profile for each model with an aim of differentiating the plate models from the half-space model and to explore spatial variations of the plate thickness of the SAFS.

For profile a that crosses the Brawley Seismic Zone to the south of the Salton Sea in Southern California, the thin plate model yields the best fit to the GPS data at a RMS of 2.85 mm/yr. Our fault geometry is based on the seismicity location in the crust even though there is no evidence of surface breaks of an active fault. The model fit to the velocities is good to the west of the Brawley Seismic Zone but gets worse to the east. The Coachella segment of the San Andreas Fault and the San Jacinto fault (profile b) is fit within an RMS of ~ 1.4 mm/yr for all the three models. Profiles c and d suggest that over the San Bernardino Mountain region, the geodetic data favor the thick plate model. The residuals 100 km to the east of the SAF are likely due to unmodeled postseismic signals from either the Landers or the Hector Mine earthquakes. The GPS velocities are matched well by the half-space model (RMS = 1.56 mm/yr) and the thick plate model (RMS = 1.61 mm/yr) at the Mojave segment (e), while the thin plate model gives a misfit of 1.77 mm/yr, slightly worse than the other models. At the northern tip of the Mojave segment (profile f), the difference in the plate thickness becomes more evident; the RMS misfit of the thin plate model is 0.2 mm/yr greater than the thick plate model. It is worth noting that approximately 50 km on either side from the SAF, the thin plate model predicts slower velocities than what is observed by GPS. GPS observations provide evidence for the existence of a relatively thick (~60 km) plate underneath the Mojave segment. Profile g crossing the central section of the Cholame-Carrizo segment of the SAF reflects a strong asymmetry of the GPS velocities, as previously noted by *Schmalzle et al.* [2006]. We tested an alternative fault geometry (i.e., dipping fault) and discuss the results of this in section 6.3. For profile h, there is no longer an asymmetry in GPS velocities.

For profile i that transects the locked portion of the Parkfield segment, we infer that the thin plate model fits the GPS observations best with an RMS of 1.82 mm/yr. This result suggests the existence of anomalous lithospheric structure underneath Parkfield. From profile j, it seems that the half-space model more appropriately represents the creeping section, and no earthquake cycle model is needed at the central portion of the creeping section to explain the present-day GPS velocities. For the profile k that crosses the Santa Cruz Mountain, there are two closely spaced paralleling creeping faults, the San Andreas Fault and the Calaveras Fault. They are well resolved by our model because of the constraints provided by InSAR. The thick plate model provides the best fit (RMS = 1.34 mm/yr). The GPS data are fit almost perfectly at profile l crossing the southern portion of the Peninsular segment of the SAF. The two steps in the velocity are due to aseismic creep of the Hayward and Calaveras faults. At the north portion of the Peninsular segment (profile m), the thick plate model produces the best fit (RMS = 1.51 mm/yr), compared to 1.68 mm/yr RMS from the half-space model and 1.61 mm/yr RMS from the thin plate. At profile n that crosses the North Coast segment and the Rodgers Creek fault, the half-space model predicts significantly larger misfit than the plate models (RMS = 1.77 mm/yr versus 1.60 mm/yr). Aseismic creep is recovered along the Rodgers Creek fault and the Hunting Creek-Bartlett Springs fault.

Among all the profiles, the last two profiles o and p crossing the North Coast and the Maacama fault are the most intriguing ones. Due to lack of constraints, the three models we tested predict drastically different secular velocities. Our models deduce significant aseismic creep on both of the Maacama and the Bartlett Springs fault. There is little shear motion within the crustal block between the Maacama and Bartlett Springs fault as constrained by the four GPS sites (between 425 km and 475 km) in profile o. To the north, however, profile p reveals uniform shear. From profile p, the RMS misfit favors the thick plate model (2.06 mm/yr). These models should be reevaluated when more accurate geodetic data become available.

In summary, an analysis of the 16 GPS velocity profiles and the earthquake cycle models across the entire SAFS suggests that the thick plate (60 km) is usually a better representation in California, with exceptions at

three important locations: the Brawley Seismic Zone, the Parkfield segment, and the creeping section. The modeling favors a relatively thin (30 km) elastic plate near the Brawley Seismic Zone and the Parkfield segment. The half-space model is preferred over the earthquake cycle models over the center portion of the creeping section of the SAF. This section is known to be devoid of large historical earthquakes, and the plate motion is mainly accommodated by aseismic creep.

5.3. Long-Term Slip Rate

Next we compared the geodetic slip rates estimated from the inversion with geologic slip rates. We incorporated the best estimate rates, as well as the upper and lower bounds, derived from a recent compilation of the UCERF3 geologic slip rates [*Dawson and Weldon*, 2013]. The geodetic slip rates inferred from the half-space model and three plate models (PL6019, PL3019, and PL3020) are listed separately in Table 1 and summarized in Figure 8. For illustration purposes, we also show the recovered slip rates from the HS and the PL6019 models in map view (Figure 9). First, we evaluated a general misfit between the geodetic slip rates and the best estimate geologic rates: HS (3 mm/yr), PL6019 (3 mm/yr), PL3019 (5 mm/yr), and PL3020 (4 mm/yr). From these initial comparisons, we infer that overall agreement between geology and geodesy is better for the thick plate model and the HS model.

Next, we focus our attention on key fault segments where there are significant discrepancies between the geodetic slip rates determined by the half-space model and the geologic rates. From Figure 8a and Table 1, we show that the half-space model does a reasonally good job of matching the geologic rates. However, there are two interesting anomalies: (1) the North Coast segment of the SAF has a geodetic slip rate of 14 mm/yr, much slower than the preferred geologic rate of 24 mm/yr, and (2) the Mojave segment of the SAF has a geodetic rate of 25 mm/yr, while the geologic best estimate is 34 mm/yr with rather large uncertainties (spanning 25–40 mm/yr).

We next examine the slip rates inferred from the plate models (also incorporating a variable viscosity) to see if these differences could be reconciled. From Figure 8, we found that the earthquake cycle model could resolve the discrepancy between the geodetic and geologic slip rates for both the Mojave segment and the North Coast segment of the SAF. The thick plate model (PL6019) yields a slip rate of 23 mm/yr on the North Coast segment and a slip rate of 27.8 mm/yr of the Mojave segment. The thin plate model (PL3019) results in a higher slip rate 36.5 mm/yr along the North Coast segment and 33.1 mm/yr along the Mojave segment. It can be seen that the plate thickness plays a key role in the recovered geodetic slip rate. For the North Coast segment, the thick plate model is the best in terms of matching the geologic slip rates, but for the Mojave segment, the thin plate model is preferred. The effects of the viscosity on the recovered slip rates can be interpreted by comparing Figures 8c and 8d. For the Mojave segment, for example, increasing the mantle viscosity from 10^{19} Pa s to 10^{20} Pa s results in a dramatic decrease in the geodetic slip rates from 33.1 to 22.9 mm/yr. Similarly, for the North Coast segment, the viscosity change results in a reduction in the slip rate estimation from 36.5 to 33.2 mm/yr.

Because of time-dependent viscoelastic relaxation effects, the interseismic velocity in the early earthquake cycle is always faster than the cycle average [*Savage and Prescott*, 1978]. Likewise, the interseismic velocity in the late cycle is always slower than the cycle average (Figure 3). The recovered slip rates for the plate models are strongly influenced by the time at which each fault is in its earthquake cycle. The last event that occurred on the North Coast segment of the SAFS was the 1906 San Francisco earthquake and the last event on the Mojave segment was the 1857 Fort Tejon earthquake. Given a recurrence interval of 200 years, both the Mojave section and the North Coast section of the SAF are late in the earthquake cycle, so to fit the observed velocities, the models require higher fault slip rate. The earthquake cycle effect gets stronger as the elastic plate gets thinner. The response time of the earthquake cycle effects are determined by the half-space viscosity: a high viscosity implies a longer response time than a low viscosity.

We compared our results with recent findings by *Chuang and Johnson* [2011] and *Hearn et al*. [2013]. Both of these detailed studies focused on the discrepancy along the Mojave segment in Southern California. *Chuang and Johnson* [2011] estimated a slip rate of 26 mm/yr along the Mojave segment assuming a three-layer model. *Hearn et al*. [2013] deduced the slip rates of the Mojave segment to be 27–29 mm/yr, assuming a four-layer rheological model. Our results, compared to these previous results, shed new light on the importance of the rheology in estimating the slip rate parameters. Because the elastic plate thickness depends on the temporal characteristics of loading, the elastic thickness inferred from the earthquake cycles should be much

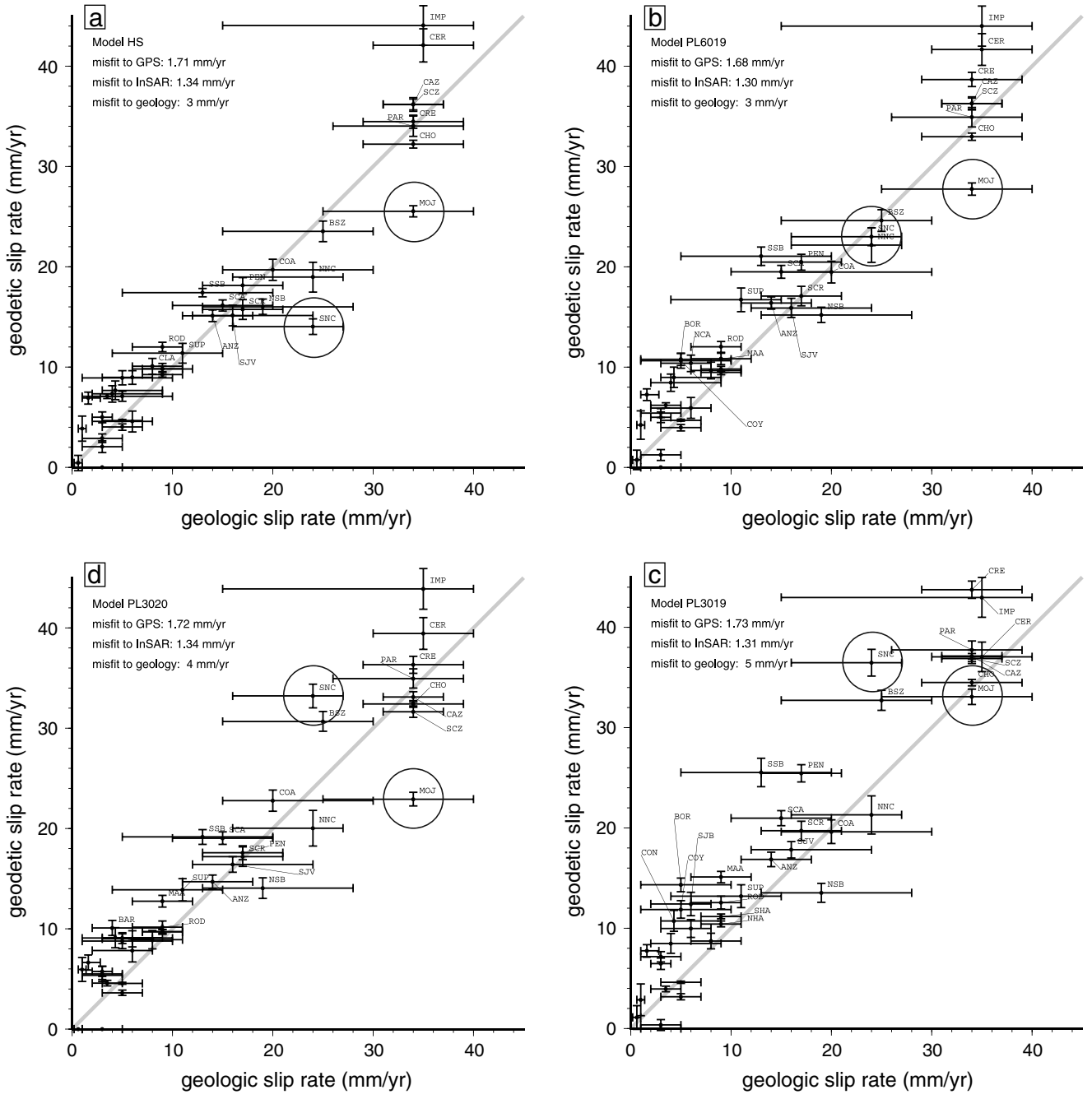

Figure 8. Geodetic slip rates in comparison to the geological slip rates. The 3-character labels for fast slipping fault segments (slip rates > 10 mm/yr) are shown (Figure 1, Table 1). The horizontal error bars represent the upper and lower bounds of the geological estimates, the vertical error bars represent the uncertainties estimated in the slip rate inversion. The overall RMS misfits to the GPS, InSAR, and preferred geological slip rates are shown in the upper left. (a) Geodetic slip rates determined by the HS model. (b) Geodetic slip rates determined by the PL6019 model. (c) Geodetic slip rates determined by the PL3019 model. (d) Geodetic slip rates determined by the PL3020 model. The recovered slip rates on key fault segments (Mojave and the North Coast segment of the SAF) are highlighted by circles.

greater than the ones inferred from the isostatic rebound or gravity studies [*Watts*, 2007]. Using a plate model and varying the elastic thickness of the plate, we demonstrated that the earthquake cycle model could agree with the geologic slip rates of 34 mm/yr along the Mojave segment if the elastic plate is relatively thin (30 km) and the half-space viscosity is 10^{19} Pa s. We haven't found other geophysical evidence that supports an unusually thin elastic plate near the Mojave segment. Another possibility is that the geological slip rate of the Mojave segment is overestimated by about 6 mm/yr.

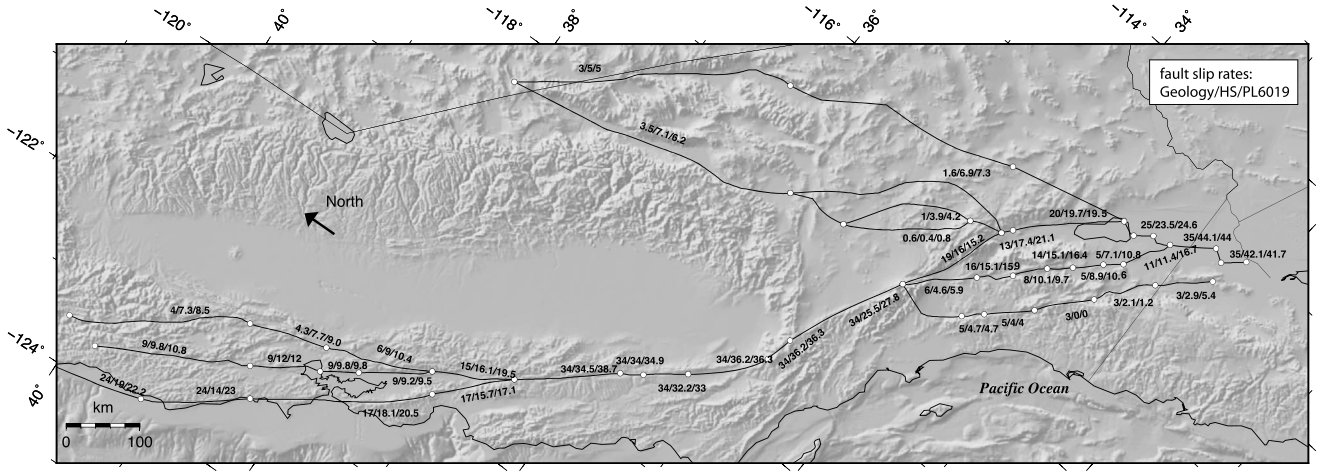

Figure 9. A summary of the recovered geodetic slip rates (mm/yr) in map view. Provided for each label is the geological fault slip rate, the geodetic slip rate determined from the HS model, and the geodetic slip rate determined from the PL6019 model. See also Figures 1 and 8.

We note that there are other anomalies between the half-space rates and the geologic rates, which our earthquake cycles models cannot explain. The geodetic slip rates of the Imperial fault and the Cerro Prieto Fault are 10 mm/yr faster than the geologic estimates of 35 mm/yr. The Lenwood-Lockhart-Old Woman Springs fault and Calico-Hidalgo fault in the Mojave Desert are also significantly faster than the geologic rates. The causes of these inadequacies are probably due to poor geodetic coverage and poor knowledge about the fault structures and the chronological sequence of the past events in those regions.

6. Discussions

6.1. Past Earthquakes Assumption

In this study, the timing of past events are derived from a compilation of historical and prehistorical earthquake records [*Smith and Sandwell*, 2006, and references therein]. We assume that the coseismic slip of past events completely releases the slip deficit accumulated since the last event. This assumption originates from the elastic rebound theory which is probably correct over geological time scales. However, it is rather difficult to collect a complete record of all the past earthquakes. There might be significant deviations from a periodic behavior over a time span of several earthquake cycles. For example, a study from *Sieh et al.* [2008] implied earthquake supercycles since past 700 years at the Sumatra subduction zone.

Here we investigated the effect of past events on the geodetic slip rate using the Mojave segment of the SAF as an example. The Mojave segment has experienced the 1812 Wrightwood-Santa Barbara earthquake ($M = 7.5$) and the 1857 Fort Tejon earthquake ($M7.9$). Prehistorical earthquakes since the year 1000 A.D. are estimated to have occurred around years 1016, 1116, 1263, 1360, 1487, 1536, and 1685. Under the slip-predictable model assumption, the slip magnitude of the 1812 event is 2.8 times greater than the 1857 event. Since the transient velocity from the postseismic relaxation is proportional to the magnitude of the coseismic slip, the postseismic contribution following the 1857 rupture is 2.8 times smaller than the 1812 rupture.

We tested the effect of the 1857 rupture on the present-day velocities by considering three scenarios: (a) increasing the coseismic slip of the 1857 event by a factor of 4, (b) removing the 1857 event from the earthquake sequence, and (c) adding a synthetic earthquake in 1957 on this segment. The new slip rates of the Mojave segment are shown in Table 3. Scenario a and b show that the magnitude of the 1857 event has

Table 3. Effect of the 1857 Fort Tejon Earthquake on the Recovered Geodetic Slip Rates Along the Mojave Segment of the SAFS (See Text for Details)

Scenarios on the Mojave Segment	Scenario A	Scenario B	Scenario C	No Change
PL6019 model slip rate (mm/yr)	27.5	27.8	26.4	27.8
PL3019 model slip rate (mm/yr)	32.5	33	28.4	33
PL3020 model slip rate (mm/yr)	20.8	23.6	20.8	22.9

little effects on the slip rate estimation for a viscosity of 10^{19} Pa s. For a viscosity of 10^{20} Pa s, magnifying the 1857 postseismic signal by a factor of 4 can decrease the slip rate estimate by ~2 mm/yr; removing the 1857 event can increase the slip rate estimate by ~1 mm/yr. Scenario c shows that the slip rate could be underestimated systematically, depending on viscosity, if the timing of the last event is set to be later than its real occurrence.

We found that the influence of the slip-predictable hypothesis to the geodetic slip rates is not significant, given a moderate viscosity of the substrate. However, it is important to estimate the timing of the most recent events in order to determine whether the earthquake cycle is in an early or late stage. It should be noted that the slip magnitude of previous events is needed if one wants to evaluate the absolute magnitude of stress in the lithosphere. *Hetland and Hager* [2006] considered such a model to investigate the influence of the initial stress on the interseismic strain accumulation.

As pointed out by *Hearn et al*. [2013], the postseismic effect resulting from a single earthquake is different from the long-lived transient effect resulted from multiple earthquake cycles. For a finite length rupture in three-dimensions, as considered in our model, the postseismic effect is limited to a distance that is approximately the rupture length. However, the cumulative earthquake cycle effect from all past events reaches beyond the rupture length. This is because the viscoelastic relaxation effect is no longer resultant from one particular fault segment but rather the contributions from all the other fault segments in the region. This effect highlights the importance of incorporating realistic past earthquake sequences into three-dimensional earthquake cycle models.

6.2. Spatial Variations in Elastic Plate Thickness Inferred From Secular GPS Velocities

For the plate models, the deformation beneath the elastic layer within the lower crust and upper mantle is distributed by ductile flow. The viscosity of the lower crust/upper mantle was found to be 9.5×10^{19} Pa s [*Kenner and Segall*, 2003] using post-1906 earthquake deformation data. Studies following earthquakes occurring in the Mojave Desert suggest time-dependent mantle rheology consistent with transient behavior [*Pollitz et al*., 2001; *Freed and Bürgmann*, 2004; *Freed et al*., 2010]. Because the rheological properties underneath California are not known, we experimented with an effective viscosity of 10^{19} Pa s and 10^{20} Pa s for the plate models. In earlier studies, *Hearn et al*. [2013] and *Chuang and Johnson* [2011] assumed different elastic layer thicknesses and a more sophisticated viscosity structure representing lower crust, uppermost mantle, and the asthenosphere. *Chuang and Johnson*'s [2011] model consists of 20 km elastic plate, 10 km thick lower crust with a viscosity of 2×10^{20} Pa s and a half-space viscosity of 6×10^{18} Pa s. *Hearn et al*.'s [2013] model consists of 25 km elastic plate, 5 km thick lower crust with a viscosity of 3×10^{19} Pa s, 20 km uppermost mantle with a viscosity of 10^{21} Pa s, and a half-space viscosity of 3×10^{18} Pa s. It has yet to be determined whether the lower crust or the uppermost mantle has stronger viscous strength in supporting the tectonic stress [*Bürgmann and Dresen*, 2008]. In this study, we do not intend to differentiate the lower crust from the uppermost mantle. There are trade-offs between the elastic thickness and the effective viscosity below [*Watts*, 2007] and biases in the estimates of viscosity [*Hines and Hetland*, 2013]. In general, a thicker elastic plate implies higher viscosity in the lower crust and the uppermost mantle.

Along the SAFS where the fault geometry is simple, the effect of the plate thickness on the internal elastic strain within the blocks is readily discernable (Figures 7g and 7h). The plate model produces prominent interseismic strain within internal elastic blocks away from the fault in contrast to the half-space model. The amount of internal elastic strain distributed within the block increases as the elastic plate thickness decreases. This can be seen clearly that the thin plate model predicts significantly slower secular velocities ~50 km away from the SAF than the thick plate model. In the far-field, at distances greater than ~100 km away from the fault, velocities inferred from the aforementioned three models are essentially indistinguishable. We deduce the effective elastic thickness to be 60 km over the Cholame-Carrizo segment.

Currently, there is no consensus on the heterogeneity of the effective plate thickness of California at earthquake cycle time scales (~10–1000 years). Previous studies using viscoelastic earthquake cycle models generally assume that the rheological structure underneath California is uniform everywhere. *Smith and Sandwell* [2006] deduced an overall elastic thickness of 70 km for the SAFS, in good agreement with 44–100 km found by *Johnson and Segall* [2004]. In this study, we attempted to probe the spatial variations of the elastic thickness using precise secular GPS velocity. By carefully examining 16 GPS velocity profiles, we

infer that the elastic thickness is generally large (~60 km) over most of the SAFS but is relatively small (~30 km) near the Brawley Seismic Zone and the Parkfield. Our finding is in line with a recent study which found an anomalously thin lithosphere beneath the Salton Trough using teleseismic receiver functions [*Lekic et al*., 2011]. In addition, these results are consistent with vertical rebound modeling results from the unloading of Lake Cahuilla due to the evaporation ~300 years ago (35 km, 10^{19} Pa s) [*Luttrell et al*., 2007]. The anomalously thin elastic layer implies low effective viscosity in the lower crust/uppermost mantle, which could be caused by localized thinning of the lithosphere due to high heat flux or the presence of partial melt or fluid. The elastic thickness from the surface deformation measurements should also be distinguished from those inferred from gravity anomalies. The elastic thickness in California inferred from gravity (~15 km) [*Lowry et al*., 2000] is much lower than what we inferred in this study, possibly due to longer time scales sampled by gravity [*Thatcher and Pollitz*, 2008].

6.3. Effect of Dipping Fault Geometry

From Figures 7a–7h, the GPS velocity data along the central Carrizo segment appear asymmetric across the SAF. It is possible that our slip rate inversion could be biased by inaccurate representation of fault geometry. It has been proposed that the geometry of the SAF is significantly different from vertical. In the southern SAF near the Coachella Valley, the fault is dipping toward the northeast, and near the "Big Bend" region, the fault is dipping toward the southwest [*Fuis et al*., 2012; *Lindsey and Fialko*, 2013], where the overall shape of the fault surface is similar to a "propeller." The dipping geometry can be further tested using deformation models because a dipping fault will shift the center of the strain concentration, which is observable in geodetic data. The gravity and electromagnetic data suggest that the Carrizo segment maybe dipping to the west at 60°. We tested this dipping fault hypothesis using local GPS velocity data and the elastic half-space model. The GPS data within 10 km from profile *g* shown in Figures 7a–7h were used in evaluating the model misfit. As shown in Figures 7a–7h, the deformation model with the SAF dipping to the west remarkably reduces the RMS misfit of the GPS data from 1.7 mm/yr to 0.96 mm/yr. This model comparison suggests that the dipping SAF hypothesis is supported by the geodetic data. An alternative explanation of the asymmetric strain at the Carrizo segment is through laterally varying crustal properties [*Schmalzle et al*., 2006]. In their model, a weak zone with 10–25 km width to the northeast of the SAF is required to explain the observed GPS velocity.

7. Conclusions

Since long-term slip rates estimated from geology are subject to uncertainties, the present-day geodetic measurements have been employed to estimate slip rates. We investigated the geodetic slip rates of the SAFS using both a viscoelastic earthquake cycle model and an elastic half-space model and compared these results with geologic slip rates. Incorporating 1981 GPS velocity vectors, 53,792 InSAR velocity points, and comprehensive geological information into a constrained least squares problem, we examined 41 fault segments along the SAFS to identify anomalous geodetic slip rates. We found that the geodetic slip rates from an elastic half-space model are significantly lower than the geologic estimates along the North Coast segment and the Mojave segment of the SAF by about 10 mm/yr. This apparent discrepancy can be reconciled by introducing time-dependent deformation governed by the viscoelastic earthquake cycle effect. In this regard, the viscoelastic cycle model is more realistic compared to the elastic half-space model.

The influence of the earthquake cycle on geodetic slip rates depends strongly on past earthquakes and the rheology of the lower crust and upper mantle. In the context of a two-layer viscoelastic model, a 60 km thick elastic plate with viscosity of 10^{19} Pa s provides the best fit to the geodetic and geological data. It is observed that the earthquake cycle effect gets stronger as the elastic plate gets thinner. For the Mojave segment (geologic rate of 34 mm/yr), the inferred geodetic slip rate is 27.8 mm/yr for the thick plate model and is 33.1 mm/yr for the thin plate model. For the North Coast segment (geologic rate of 24 mm/yr), the inferred geodetic slip rate is 23 mm/yr for the thick plate model and is 36.5 mm/yr for the thin plate model. We identified discrepancies on other faults along the SAFS such as the Imperial fault, the Cerro Prieto Fault, and the faults in the East California Shear Zone, which cannot be explained by the viscoelastic effect. Finally, we found that the influence of the slip-predictable hypothesis to the recovered geodetic slip rates is not significant.

Acknowledgments
This work was supported by NSF grant EAR-1147427 (EarthScope) and EAR-0847499, EAR-1147435, and EAR-0838252. We are grateful to Tom Herring, Yuehua Zeng, and ZhengKang Shen for useful discusssions and suggestions. We thank Eric Hetland and an anonymous reviewer for reviewing our manuscript and their helpful comments. Tom Herring provided the GPS data used in the study (Herring, T.A., K.H. Ji, and R.W. King, 711 "Geodetic Modeling and Transient Detection using SCIGN and PBO data", SCEC-3 Final report, USC, 2012. http://sceccore2.usc.edu/proposal-files/2011reports/Herring_11078_report.pdf). GPS data are from the Plate Boundary Observatory (PBO) operated by UNAVCO for EarthScope (http://www.earthscope.org) and supported by NSF grant EAR-0323309 and the Southern California Integration GPS Network (SCIGN) operated by USGS/Pasadena and SOPAC. Data products were used from Yehuda Bock and Frank Webb 2012: NASA MEASUREs Solid Earth Science ESDR System, La Jolla, California, and Pasadena, California, through the GPS Explorer data portal (http://geoapp.ucsd.edu/). The InSAR data in Figure 2 [*Tong et al.*, 2013] are available in the supporting information of this paper. The figures are produced by Generic Mapping Tools (GMT) [*Wessel et al.*, 2013].

References

Bird, P. (2009), Long-term fault slip rates, distributed deformation rates, and forecast of seismicity in the western United States from joint fitting of community geologic, geodetic, and stress direction data sets, *J. Geophys. Res.*, *114*, B11403, doi:10.1029/2009JB006317.

Bock, Y., et al. (2011), Evaluation of transient deformation from two decades of continuous GPS time series analysis in Western North America, *Eos Trans. AGU, 91*, Fall Meet. Suppl., Abstract G53C-01.

Bürgmann, R., and G. Dresen (2008), Rheology of the lower crust and upper mantle: Evidence from rock mechanics, geodesy and field observations, *Ann. Rev. Earth Plan. Sci.*, *36*, 531–567, doi:10.1146/annurev.earth.36.031207.124326.

Chuang, R. Y., and K. M. Johnson (2011), Reconciling geologic and geodetic model fault slip-rate discrepancies in Southern California: Consideration of nonsteady mantle flow and lower crustal fault creep, *Geology*, *39*(7), 627–630, doi:10.1130/G32120.32121.

Crowell, B. W., Y. Bock, D. T. Sandwell, and Y. Fialko (2013), Geodetic investigation into the deformation of the Salton Trough, *J. Geophys. Res. Solid Earth*, *118*, 5030–5039, doi:10.1002/jgrb.50347.

Dawson, T. E. and R. J. Weldon II (2013), Appendix B of uniform California earthquake rupture forecast, Version 3 (UCERF3): Geologic slip-rate data and geologic deformation model, U.S. Geol. Surv., Menlo Park, California, U.S.A.

Dixon, T., J. Decaix, F. Farina, K. Furlong, R. Malservisi, R. A. Bennett, F. Suarez-Vidal, J. Fletcher, and J. Lee (2002), Seismic cycle and rheological effects on estimation of present-day slip rates for the Agua Blanca and San Miguel-Vallecitos faults, northern Baja California, Mexico, *J. Geophys. Res.*, *107*(B10), 2226, doi:10.1029/2000JB000099.

Dixon, T. H., E. Norabuena, and L. Hotaling (2003), Paleoseismology and Global Positioning System: Earthquake-cycle effects and geodetic versus geologic fault slip rates in the eastern California shear zone, *Geology*, *31*, 55–58, doi:10.1130/0091-7613.

Fialko, Y. (2004), Probing the mechanical properties of seismically active crust with space geodesy: Study of the coseismic deformation due to the 1992 Mw7. 3 Landers (Southern California) earthquake, *J. Geophys. Res.*, *109*, B03307, doi:10.1029/2003JB002756.

Freed, A. M., and R. Bürgmann (2004), Evidence of power-law flow in the Mojave desert mantle, *Nature*, *430*, 548–551, doi:10.1038/nature02784.

Freed, A. M., T. Herring, and R. Bürgmann (2010), Steady-state laboratory flow laws alone fail to explain postseismic observations, *Earth Planet. Sci. Lett.*, *300*, 1–10, doi:10.1016/j.epsl.2010.10.005.

Fuis, G. S., D. S. Scheirer, V. E. Langenheim, and M. D. Kohler (2012), A new perspective on the geometry of the San Andreas Fault in Southern California and its relationship to lithospheric structure, *Bull. Seismol. Soc. Am.*, *102*(1), 236–251, doi:10.1785/0120110041.

Geist, E. L., and D. J. Andrews (2000), Slip rates on San Francisco Bay area faults from anelastic deformation of the continental lithosphere, *J. Geophys. Res.*, *105*(B11), 25,543–25,552, doi:10.1029/2000JB900254.

Hearn, E. H., F. F. Pollitz, W. R. Thatcher, and C. T. Onishi (2013), How do "ghost transients" from past earthquakes affect GPS slip rate estimates on Southern California faults?, *Geochem. Geophys. Geosyst.*, *14*, 828–838, doi:10.1002/ggge.20080.

Hetland, E. A., and B. H. Hager (2006), Interseismic strain accumulation: Spin-up, cycle invariance, and irregular rupture sequences, *Geochem. Geophys. Geosyst.*, *7*, Q05004, doi:10.1029/2005GC001087.

Hetland, E. A., M. Simons, and E. M. Dunham (2010), Postseismic and interseismic deformation due to fault creep I: Model description, *Geophys. J. Int.*, *181*, 81–98, doi:10.1111/j.1365-246X.2010.04522.x.

Hines, T. T., and E. A. Hetland (2013), Bias in estimates of lithosphere viscosity from interseismic deformation, *Geophys. Res. Lett.*, *40*, 4260–4265, doi:10.1002/grl.50839.

Johnson, K. M., and P. Segall (2004), Viscoelastic earthquake cycle models with deep stress-driven creep along the San Andreas fault system, *J. Geophys. Res.*, *109*, B10403, doi:10.1029/2004JB003096.

Johnson, K. M., G. E. Hilley, and R. Burgmann (2007), Influence of lithosphere viscosity structure on estimates of fault slip rate in the Mojave region of the San Andreas fault system, *J. Geophys. Res.*, *112*, B07408, doi:10.1029/2006JB004842.

Kenner, S. J. and P. Segall (2003), Lower crustal structure in northern California: Implications from strain rate variations following the 1906 San Francisco earthquake, *J. Geophys. Res.*, *108*(B1), 2011, doi:10.1029/2001JB000189.

Lekic, V., S. W. French, and K. M. Fischer (2011), Lithospheric thinning beneath rifted regions of Southern California, *Sci. Express*, doi:10.1126/science.1208898.

Lindsey, E. O., and Y. Fialko (2013), Geodetic slip rates in the southern San Andreas Fault system: Effects of elastic heterogeneity and fault geometry, *J. Geophys. Res. Solid Earth*, *118*, 689–697, doi:10.1029/2012JB009358.

Loveless, J. P., and B. J. Meade (2011), Stress modulation on the San Andreas fault by interseismic fault system interactions, *Geology*, *39*(11), 1035–1038, doi:10.1130/G32215.1.

Lowry, A. R., N. M. Ribe, and R. B. Smith (2000), Dynamic elevation of the Cordillera, western United States, *J. Geophys. Res.*, *105*(B10), 23,371–23,390, doi:10.1029/2000JB900182.

Lundgren, P., E. A. Hetland, Z. Liu, and E. J. Fielding (2009), Southern San Andreas-San Jacinto fault system slip rates estimated from earthquake cycle models constrained by GPS and interferometric synthetic aperture radar observations, *J. Geophys. Res.*, *114*, B02403, doi:10.1029/2008JB005996.

Luttrell, K., D. Sandwell, B. Smith-Konter, B. Bills, and Y. Bock (2007), Modulation of the earthquake cycle at the southern San Andreas fault by lake loading, *J. Geophys. Res.*, *112*, B08411, doi:10.1029/2006JB004752.

McCaffrey, R. (2005), Block kinematics of the Pacific-North America plate boundary in the southwestern United States from inversion of GPS, seismological, and geologic data, *J. Geophys. Res.*, *110*, B07401, doi:10.1029/2004JB003307.

McGill, S. F., L. A. Owen, R. J. Weldon II, and K. J. Kendrick (2013), Latest Pleistocene and Holocene slip rate for the San Bernardino strand of the San Andreas fault, Plunge Creek, Southern California: Implications for strain partitioning within the southern San Andreas fault system for the last ~35 k.y, *Geol. Soc. Am. Bull.*, *125*(1–2), 48–72, doi:10.1130/B30647.1.

Meade, B. J., and B. H. Hager (2005), Spatial localization of moment deficits in Southern California, *J. Geophys. Res.*, *110*, B04402, doi:10.1029/2004JB003331.

Nur, A., and G. Mavko (1974), Postseismic viscoelastic rebound, *Science*, *183*(4121), 204–206, doi:10.1126/science.183.4121.204.

Oskin, M., L. Perg, E. Shelef, M. Strane, E. Gurney, B. Singer, and X. Zhang (2008), Elevated shear zone loading rate during an earthquake cluster in eastern California, *Geology*, *36*, 507–510, doi:10.1130/G24814A.24811.

Pollitz, F. F., C. Wicks, and W. Thatcher (2001), Mantle flow beneath a continental strike-slip fault: Postseismic deformation after the 1999 Hector Mine earthquake, *Science*, *293*(5536), 1814–1818, doi:10.1126/science.1061361.

Pollitz, F., W. H. Bakun, and M. Nyst (2004), A physical model for strain accumulation in the San Francisco Bay region: Stress evolution since 1838, *J. Geophys. Res.*, *109*, B11408, doi:10.1029/2004JB003003.

Rolandone, F., R. Bürgmann, D. C. Agnew, I. A. Johanson, D. C. Templeton, M. A. D'alessio, S. J. Titus, C. Demets, and B. Tikoff (2008), Aseismic slip and fault-normal strain along the central creeping section of the San Andreas fault, *Geophys. Res. Lett.*, *35*, L14305, doi:10.1029/2008GL034437.

Savage, J. C., and M. Lisowski (1998), Viscoelastic coupling model of the San Andreas fault along the Big Bend, Southern California, *J. Geophys. Res.*, *103*(B4), 7281–7292, doi:10.1029/98JB00148.

Savage, J., and W. Prescott (1978), Asthenosphere readjustment and the earthquake cycle, *J. Geophys. Res.*, *83*(B7), 3369–3376, doi:10.1029/JB083iB07p03369.

Schmalzle, G., T. Dixon, R. Malservisi, and R. Govers (2006), Strain accumulation across the Carrizo segment of the San Andreas Fault, California: Impact of laterally varying crustal properties, *J. Geophys. Res.*, *111*, B05403, doi:10.1029/2005JB003843.

Shen, Z.-K., R. King, D. Agnew, M. Wang, T. Herring, D. Dong, and P. Fang (2011), A unified analysis of crustal motion in Southern California, 1970–2004: The SCEC crustal motion map, *J. Geophys. Res.*, *116*, B11402, doi:10.1029/2011JB008549.

Sieh, K., D. H. Natawidjaja, A. J. Meltzner, C. C. Shen, H. Cheng, K. S. Li, B. W. Suwargadi, J. Galetzka, B. Philibosian, and R. L. Edwards (2008), Earthquake supercycles inferred from sea-level changes recorded in the corals of west Sumatra, *Science*, *322*(5908), 1674–1678, doi:10.1126/science.1163589.

Smith, B., and D. Sandwell (2004), A three-dimensional semianalytic viscoelastic model for time-dependent analyses of the earthquake cycle, *J. Geophys. Res.*, *109*, B12401, doi:10.1029/2004JB003185.

Smith, B., and D. T. Sandwell (2006), A model of the earthquake cycle along the San Andreas Fault system for the past 1000 years, *J. Geophys. Res.*, *111*, B01405, doi:10.1029/2005JB003703.

Smith-Konter, B., and D. Sandwell (2009), Stress evolution of the San Andreas Fault System: Recurrence interval versus locking depth, *Geophys. Res. Lett.*, *36*, L13304, doi:10.1029/2009GL037235.

Smith-Konter, B., D. T. Sandwell, and P. Shearer (2011), Locking depths estimated from geodesy and seismology along the San Andreas Fault System: Implications for seismic moment release, *J. Geophys. Res.*, *116*, B06401, doi:10.1029/2010JB008117.

Solis, T. (2013), Estimating variations in locking depth for the Mojave segment of the San Andreas fault over the past 1500 years from paleoseismic stress drop, MS thesis, University of Texas at El Paso, El Paso, Tex.

Spinler, J. C., R. A. Bennett, M. L. Anderson, S. F. McGill, S. Hreinsdottir, and A. McCallister (2010), Present-day strain accumulation and slip rates associated with southern San Andreas and Eastern California shear zone faults, *J. Geophys. Res.*, *115*, B11407, doi:10.1029/2010JB007424.

Thatcher, W., and F. F. Pollitz (2008), Temporal evolution of continental lithospheric strength in actively deforming regions, *GSA Today*, *18*, 4–11, doi:10.1130/GSAT01804-5A.1.

Titus, S. J., C. Demets, and B. Tikoff (2006), Thirty-five-year creep rates for the creeping segment of the San Andreas Fault and the effects of the 2004 Parkfield earthquake: Constraints from alignment arrays, continuous Global Positioning System, and creepmeters, *Bull. Seismol. Soc. Am.*, *96*(4), S250–S268, doi:10.1785/0120050811.

Toké, N. A., J. R. Arrowsmith, M. J. Rymer, A. Landgraf, D. E. Haddad, M. Busch, J. Coyan, and A. Hannah (2011), Late Holocene slip rate of the San Andreas fault and its accommodation by creep and moderate-magnitude earthquakes at Parkfield, *Calif. Geol.*, *39*, 243–246, doi:10.1130/G31498.1.

Tong, X., D. Sandwell, and B. Smith-Konter (2012), A systematic estimation of fault creep rates along major faults in California from L-band radar interferometry, 205, presented at 2012 Annual Meeting of Southern California Earthquake Center, Univ. Southern California/Southern California Earthquake Center, Palm Springs, California, 9–12 Sept.

Tong, X., D. Sandwell, and B. Smith-Konter (2013), High-resolution interseismic velocity data along the San Andreas Fault from GPS and InSAR, *J. Geophys. Res. Solid Earth*, *118*, 369–389, doi:10.1029/2012JB009442.

van der Woerd, J., Y. Klinger, K. Sieh, P. Tapponnier, F. J. Ryerson, and A.-S. Mériaux (2006), Long-term slip rate of the southern San Andreas Fault from 10Be-26Al surface exposure dating of an offset alluvial fan, *J. Geophys. Res.*, *111*, B04407, doi:10.1029/2004JB003559.

Wang, R., F. L. Martın, and F. Roth (2003), Computation of deformation induced by earthquakes in a multi-layered elastic crust—Fortran programs edgrn/edcmp, *C. R. Geosci.*, *29*(2), 195–207, doi:10.1016/S0098-3004(02)00111-5.

Watts, A. B. (2007), Crust and lithosphere dynamics: An overview, in *Treatise on Geophysics*, edited by G. Schubert, pp. 1–48, Elsevier, Amsterdam, ISBN: 978-0-444-53462-0.

Wdowinski, S., B. Smith-Konter, Y. Bock, and D. Sandwell (2007), Diffuse interseismic deformation across the Pacific–North America plate boundary, *Geology*, *35*(4), 311–314, doi:10.1130/G22938A.1.

Wessel, P., W. H. F. Smith, R. Scharroo, J. F. Luis, and F. Wobbe (2013), Generic mapping tools: Improved version released, *EOS Trans. AGU*, *94*, 409–410, doi:10.1002/2013EO450001.

Zeng, Y., and Z. K. Shen (2014), Fault network modeling of crustal deformation in California constrained using GPS and geologic observations, *Tectonophysics*, *612–613*, 1–17, doi:10.1016/j.tecto.2013.11.030.